| Author(s) | Collaborating Institution |
|---|---|
| D. Arbelaez | |


| Reviewed By | Reviewed Date |
|---|---|
| | |

| Approved / Concurred By | DCC Release Date |
|---|---|
| | |

Title
LCLS-II-HE SXR Undulator: Magnetic Design Report

# LCLS-II-HE SXR Undulator: Magnetic Design Report

## 1. Contents



## 2. Revision History

| Revision | Issued | Changes |
|---|---|---|
| A | 01-26-2021 | Original issue. |

# 3. Purpose

This document describes the magnetic design for the soft x-Ray (SXR) undulators for the high energy upgrade to the Linac Coherent Light Source (LCLS-II-HE). The LCLS-II is a free electron laser (FEL) that is located at the SLAC National Accelerator Laboratory. For the high energy upgrade of the LCLS-II the existing SXR undulator will be reconfigured to have a longer period length, due to the increase in electron energy from 4 to 8 GeV. The period length of the undulator will be changed from 39 mm for the original SXR undulators to 56 mm for the new SXR undulators. This is done in order to meet the minimum photon energy requirement of 250 eV with the electron energy at 8 GeV.

# 4. Scope

This document describes the magnetic design of the HE-SXR undulators. This includes the periodic magnetic design, the end design, and the tuning method analysis. For the periodic design, the basic permanent magnet block and pole dimensions are optimized to achieve the desired effective field strength while minimizing the pole saturation and the overall structure size. The reverse magnetic field on the permanent magnet blocks is evaluated to ensure that sufficient margin against demagnetization exists in the design. The roll-off of the magnetic field in the transverse direction is also evaluated to ensure that the physics requirement is satisfied. For the end design, the optimization process is described and the final results are presented. For the tuning methods, the results for expected tuning signatures are presented.

# 5. Requirements

Table 1 shows the relevant physics requirements as specified in LCLS-II-HE SXR Undulator Systems Physics Requirement Document (LCLS-II-HE-1.3-PR-0049-R0). The main parameters are the period length, the minimum gap, and the effective magnetic field requirement. With a shorter period length (approx. 54 mm) the minimum photon energy requirement (250 eV with 8 GeV electron beam) can still be satisfied, however, this will lead to highly saturated undulator poles[1]. At the same time, with increasing period length, the total undulator length required for the FEL will increase. Therefore, a period length of 56 mm was chosen as a good balance between these two constraints. In order to achieve the photon energy requirement at the minimum gap of 7.2 mm, the effective magnetic field strength needs to exceed 1.76 T.

[1] Highly saturated poles in the original SXR undulator made the tuning more time consuming. Non-linear behavior due to high saturation also increase the risk that the field quality requirements cannot be met for all undulator segments.

Table 1 shows the remaining physics requirements, which include: the operational gap range, the field repeatability requirement, the field roll-off in the transverse (x) direction, and the field quality requirements. The field quality is defined by the first and second integral requirements, as well as the phase shake (RMS phase error) requirement.

**Table 1. Physics Requirements**

| | SXR-HE Undulator Requirements |
|---|---|
| Period length [mm] | 56.0 |
| Operational gap range [mm] | 7.2 – 33.0 |
| $B_{eff}$ @ 7.2mm gap | > 1.76 T |
| ΔB/B Repeatability | $\pm 5.5 \times 10^{-4}$ |
| Field Roll-Off (ΔK/K @ x=0.4mm) | $< 1.6 \times 10^{-4}$ |
| $\lvert\int B_{x,y} dz\rvert$ | < 50 μTm |
| $\lvert\iint B_{x,y} dz^2\rvert$ | $< 200\ \mu Tm^2$ |
| Phase Shake (RMS) | < 5° |



# 6. Periodic Magnetic Design

The main objective for the periodic design is to meet the minimum effective field requirement of 1.76 T at the minimum gap of 7.2 mm. Furthermore, the poles should be wide enough to meet the field roll-off requirement as specified in Table 1. The design is also evaluated to ensure that the reverse field in the permanent magnets is low enough to provide sufficient margin to demagnetizing fields. Finally, this analysis is done under the constraint that pole saturation should be low enough to minimize the risk of tuning difficulties during production.

From the experience with tuning the LCLS-II undulators, a clear difference was seen between the HXR and SXR undulators in terms of ease of tuning. Since the HXR undulators had lower pole saturation, the tuning was faster due to the mainly monotonic behavior of the gap dependent field errors. This motivates the desire to minimize the pole saturation in the HE-SXR design. Figure 1 shows the calculated pole magnetic field strength for the LCLS-II HXR and SXR undulators. The right figure shows the location over which the magnetic field strength is determined (for the left plot) with a dashed line. This is a vertical line along the center of the pole in the ¼ period model. As can be seen from the figure, the magnetic field strength is more than an order of magnitude higher for the SXR undulator (approx. 50,000 A/m), when compared to the HXR undulator (approx. 1,000 A/m). Note that the peak saturation occurs approximately 1 to 3 mm from the surface of the pole. In

the optimization process described in the following text, a primary goal is to obtain a saturation profile along the pole center that is in line with the LCLS-II HXR design.

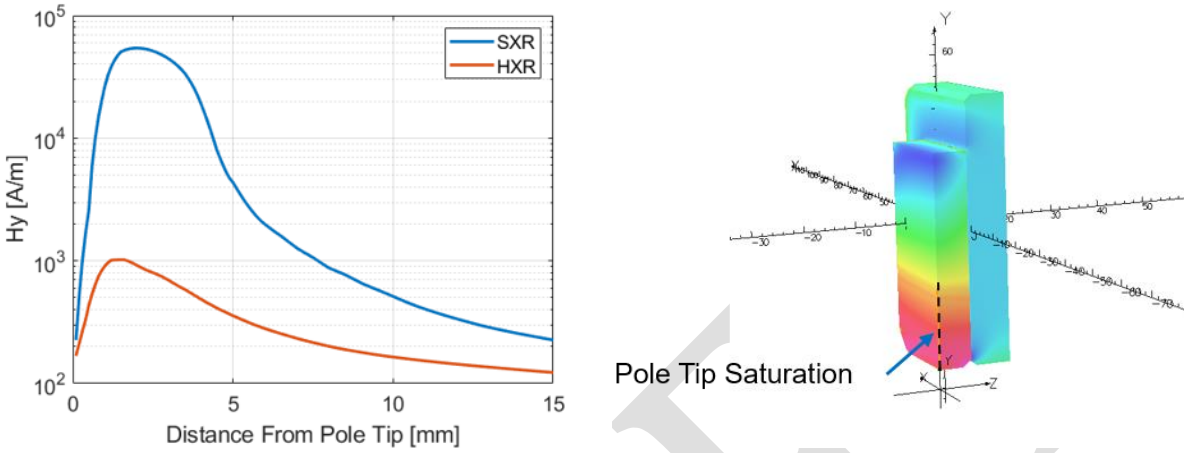


**Figure 1. Illustration of pole saturation for the LCLS-II SXR and HXR undulators. The left plot shows the magnetic field strength along a line at the center of the pole (shown in the right plot). As can be seen, the saturation of the SXR pole is significantly higher, leading to a more time consuming tuning process due to an increase in non-linear behavior of the magnetic field errors at small gap.**

## *Optimization of Permanent Magnet and Pole Dimensions*

The optimization of the pole and permanent magnet dimensions is performed using OPERA3D with a ¼ period model with ¼ symmetry in the x and y directions. The coordinate system is defined as follows: the z-direction is the beam direction, the y-direction is vertical (across the gap), and the x-direction is transverse to the gap.

The design is constrained to be compatible with the existing strongbacks. Therefore, the width of the poles and magnets can only decrease relative to the original SXR design. From a field quality standpoint, it is not desirable to decrease the pole width since it could lead to higher multipoles[2] due to magnet errors at the magnet overhangs (along the x-direction). Therefore, the pole and magnet widths are kept to approximately the same values as for the original SXR design. For the optimization of the basic pole and magnet dimensions, conservative assumptions are made on the permanent magnet performance: The permanent magnet remanence is taken to be $B_r = 1.31$ T and the reversible permeability along the easy axis direction is taken to be $\mu_{||}$=1.065. Additional

[2] There are no strict requirements on higher order multipoles, however, skew quadrupole and normal/skew sextupoles have proven to be difficult to tune over the gap range from LCLS-II experience. Therefore, it is desirable to have these be as low as possible before tuning.

features, including the pole edge chamfers and pole height adjustment wings are not included in the optimization of the basic pole and magnet dimension.

The first step in the design optimization is to determine the thickness ratio for the pole and permanent magnet. The OPERA3D analysis was performed for various values of the pole thickness ratio, $t_p/\lambda_u$, where $t_p$ is the pole thickness and $\lambda_u$ is the undulator period length. Figure 2 (left) shows the maximum field strength along the vertical pole centerline (see Figure 1) as a function of the pole thickness ratio. As expected, the pole saturation decreases significantly as the pole thickness ratio is increased. Figure 2 (right) shows the effective undulator field, $B_{eff}$, the peak on-axis field, $B_{peak}$, and the maximum magnetic flux density along the pole centerline. The effective field is defined as,

$$B_{eff} = \sqrt{\sum_m \frac{{B_m}^2}{m^2}},$$

where $B_m$ are the Fourier coefficient of the magnetic field, as a function of z, of order m. As can be seen from the plot, while the peak field decreases with increasing pole ratio thickness, the effective field reaches a maximum at a pole thickness ratio value of approximately 0.21. A pole thickness ratio of 0.23 is chosen for the design since the pole saturation is at a reasonable level and the effective field is only approximately 1% below the peak value.

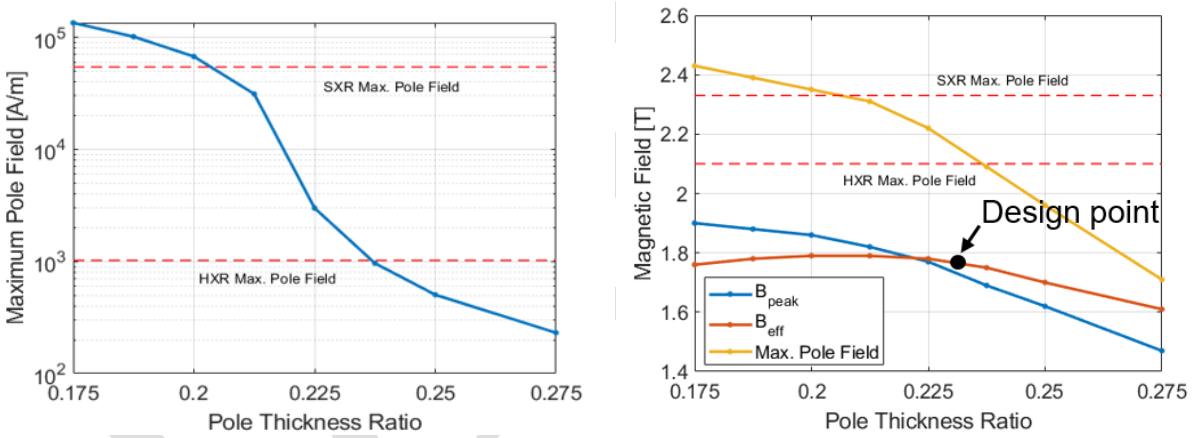


**Figure 2. Optimization of the pole thickness in order reduce pole saturation. The left plot shows the maximum magnetic field strength along the centerline of the pole as a function of pole thickness ratio. The right plot shows the change in the peak field, the effective field, and the maximum pole field as a function of pole thickness ratio. The design point is chosen such that the pole saturation is reduced significantly while the effective field is only slightly reduce relative to the maximum value.**

In order to define the pole and magnet heights, a grid of calculations was carried out by varying the pole height from 34 to 50 mm and the magnet height from 52 to 60 mm. Figure 3 shows a contour map of the magnetic field strength in the pole as a function of the pole height and magnet height. The dashed line represents contour for $B_{eff} = 1.777$ T, which is approximately 1% above the effective field requirement of 1.76 T (with conservative magnet properties). It is noteworthy, that the pole saturation contour matches closely with the effective field contour. Therefore, within the

range of magnet and pole heights considered, the pole saturation is mainly driven by the on-axis effective field strength of the undulator. The design point is chosen to minimize the overall magnetic structure height and produce a $B_{eff}$ value that is 1% above the requirement. With these constraints, the pole height is chosen to be 42 mm and the permanent magnet height is chosen to be 54 mm.

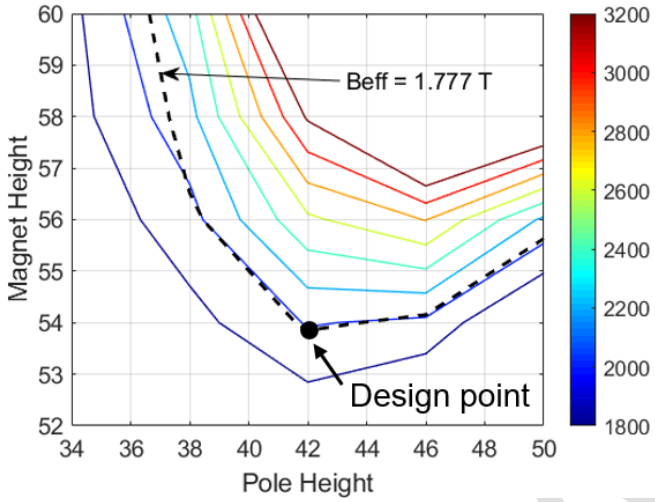


**Figure 3. Optimization of the pole and magnet heights. The heights are chosen such that an effective field margin of 1% is obtained with conservative magnet properties (shown in dashed lines). The point along the $B_{eff}$ = 1.777T contour is chosen to minimize the height of the overall structure.**

## *Pole and Magnet Chamfers and Additional Features*

In the previous section, the magnetic design was optimized relative to the basic magnet and pole dimensions. In this section, additional features are considered in the design. These include the following: long edge chamfers on the permanent magnets, short edge clamp chamfers on the permanent magnets, pole adjustment/locking features, and short and long edge chamfers on the pole. These features can be seen in Figure 4. The long edge magnet chamfers are included to remove the regions of the magnet with a high reverse magnetic field. Chamfers on the short edge of the permanent magnet are introduced as a feature to clamp the permanent magnets down on the keeper. On the poles, chamfers are included on both the short and long edges. For the short edge, the inclusion of this chamfer increased the effective field on-axis and can also reduce pole saturation. The long edge chamfer is included solely to reduce the saturation of the pole. The pole adjustment/locking features are included based on mechanical considerations and have minimal effect on the magnetic performance.

Figure 5 shows the variation in the pole saturation as a function of the effective on-axis field as the pole chamfer dimensions are varied (chamfer dimension is labeled on the data points). For the y-axis on both plots, the maximum magnetic field strength, along the vertical centerline of the pole, is used (see Figure 1). On the left graph, the effect of varying the short edge chamfer dimension is

shown, while on the right graph, the effect of varying the long edge chamfer dimension is shown. For the short edge, an increase in the chamfer size leads to an increase in the effective field of the undulator over the range examined. In terms of pole saturation, a minimum in the maximum magnetic field strength along the centerline of the pole is reached for a chamfer size of approximately 4 mm. This is the dimension that is chosen for the final configuration. For the long edge chamfer, an increase in the chamfer size leads to a decrease in the effective field strength as well as a decrease in the extent of pole saturation. There is a steep decrease in pole saturation with a moderate decrease in the effective field strength up to a chamfer size of approximately 1.0 mm. Therefore, a long edge chamfer size of 1.0 mm is chosen for the baseline design. For the analysis presented in this section, the permanent magnets are assumed to have a remanence of $B_r = 1.35$ T and the reversible permeability along the easy axis direction is taken to be $\mu_{||}$=1.04. This is in line with the values that were obtained from the LCLS-II SXR undulator production. The nominal design dimensions for the various features are given in Table 2.

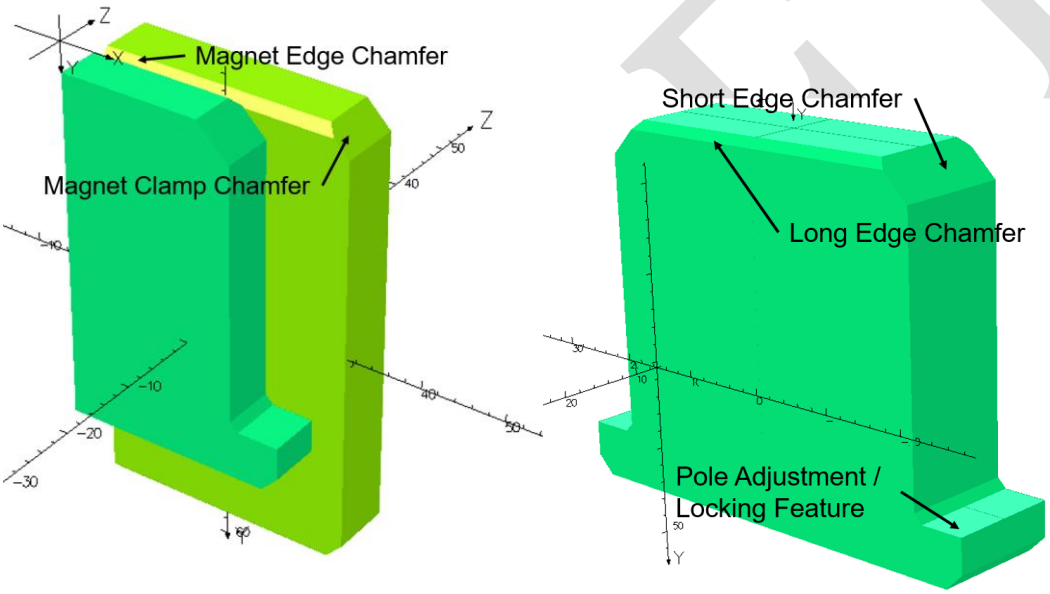


**Figure 4. Additional pole and magnet features, including: pole short and long edge chamfers, pole adjustment / locking feature, magnet long chamfer, and magnet short chamfer for clamping.**

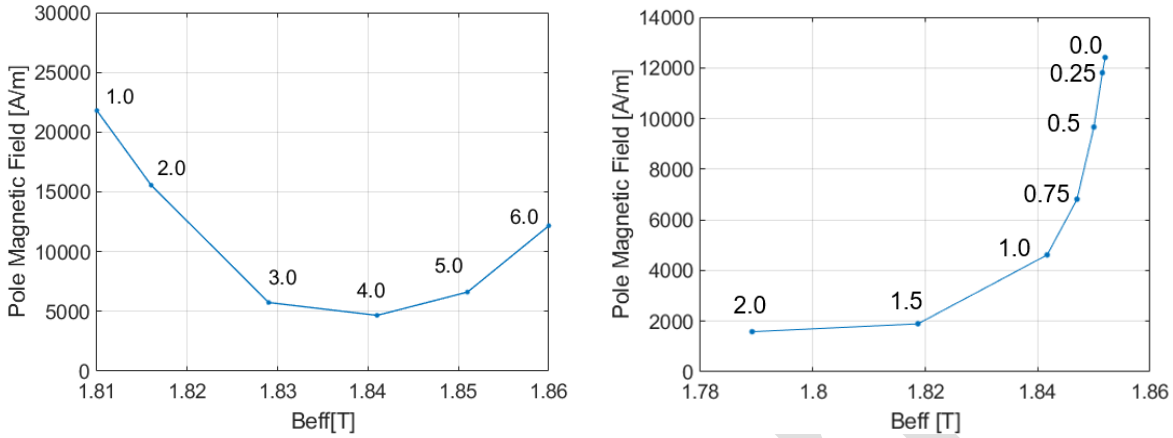


**Figure 5. Optimization of the long and short pole chamfers. The left plot shows the maximum pole magnetic field strength as a function of the on-axis effective field for the short chamfer. The right plot shows the maximum pole magnetic field strength as a function of the on-axis effective field for the long chamfer.**

**Table 2. Magnetic Design Feature Dimensions**

| Magnetic Design Feature | Value |
|---|---|
| Permanent Magnet Width [mm] | 62.0 |
| Permanent Magnet Height [mm] | 54.0 |
| Permanent Magnet Thickness [mm] | 15.0 |
| Permanent Long Edge Chamfer [mm] | 1.0 |
| Permanent Clamp Chamfer [mm] | 3.0 |
| Pole Width (excluding extension) [mm] | 42.0 |
| Pole Height [mm] | 42.0 |
| Pole Thickness [mm] | 12.88 |
| Pole Long Edge Chamfer [mm] | 1.0 |
| Pole Short Edge Chamfer [mm] | 4.0 |

## *Baseline Results and Permanent Magnet Property Sensitivity Analysis*

In this section, the results of the effective magnetic field for the baseline design are presented along with an analysis that shows the sensitivity of the effective field strength to variations in the permanent magnet properties. The goal of this analysis is to define permanent magnet specifications that provide sufficient margin for the baseline design. For the following calculations,

the minimum lateral dimensions for the permanent magnets (as specified in the fabrication drawings) are used. The air gap between the poles and the magnets is chosen to be 0.15 mm which is in middle of the allowable range based on the specified tolerances. A separate analysis using the maximum allowable air gap, between the magnet and the pole, shows a reduction of less than 0.2% in the effective field relative to the nominal case. The maximum lateral pole dimensions, as specified in the fabrication drawing, are used in the analysis. A separate analysis using the minimum lateral pole dimensions shows a negligible change in the effective field when using the minimum pole height and a small increase in effective field when using the minimum pole width.

Table 3 shows the results of the permanent magnet material property sensitivity analysis. The worst-case value for $B_r$ is chosen to be 1.32 T, while the worst case value for $\mu_{||}$ is chosen to be 1.065. The values of $B_r = 1.32$ T and $\mu_{||}$=1.065 are the worst case values, based on the LCLS-II permanent magnet specification. These values are used row 1 of Table 3, and give an effective field margin of approximately 1%. Rows 2 and 3 show values that are representative of the average as-received properties from the SXR (row 2) and HXR (row 3) production. These give an effective field margin of approximately 4.5% and 3%, respectively. This is more representative of the typical properties that are expected. The final row shows the case where the "best-case" values of Br and $\mu_{||}$ are obtained, which gives a margin of approximately 5%. Since the effective field strength is dependent on both the remanence and permeability, it is desirable to define the material property criteria so that it takes both properties into account (i.e. a lower remanence is acceptable if the permeability is also lower).

**Table 3. Results from Permanent Magnet Property Sensitivity Analysis**

| $B_r$ [T] | $\mu_{||}$ | $B_{eff}$ [T] | $H_{sat}$ [A/m] | $B_{eff}$ Margin |
|---|---|---|---|---|
| 1.32 | 1.065 | 1.776 | 1600 | 0.9% |
| 1.35 | 1.04 | 1.841 | 4700 | 4.6% |
| 1.32 | 1.03 | 1.814 | 2700 | 3.1% |
| 1.35 | 1.03 | 1.851 | 5900 | 5.2% |

The data obtained from the material property sensitivity analysis is now used to define the criteria for permanent magnet acceptance. From the results given in Table 3, the effective field of the undulator at 7.2 mm gap can be described as,

$$B_{eff}[\mathrm{T}] = 1.255 - 1.06\mu_{||} + 1.25B_r[\mathrm{T}],$$

as a function of magnet material remanence and permeability. By choosing $B_{eff}$ to be 2.5% above the required value, the following relationship between the required coercivity and remanence can be obtained:

$$H_{cB}[\mathrm{A/m}] > \frac{B_r[\mathrm{T}]}{\mu_0(1.18B_r[\mathrm{T}]-0.52)}.$$

The relationship between magnetic induction and magnetic field strength,

$$B = \mu_0\mu_{||}H + B_r,$$

has been used to derive the above $H_{cB}$ relation. Table 4 show the minimum required Coercivity that is needed to obtain a 2.5% margin on $B_{eff}$ as a function of the permanent magnet remanence. For the magnet material specification, Table 4 has been used along with the requirement that $B_r$ be greater than 1.32 T.

**Table 4. Minimum Required Coercivity to Obtain a Minimum $B_{eff}$ Margin of 2.5%.**

| $B_r$ [T] | Min $H_{cB}$ [kA/m] | Min $H_{cB}$ [kOe] | $\mu_{\|\|}$ |
|---|---|---|---|
| 1.32 | 1012 | 12.72 | 1.038 |
| 1.33 | 1009 | 12.67 | 1.050 |
| 1.34 | 1005 | 12.63 | 1.061 |
| 1.35 | 1001 | 12.58 | 1.073 |

## *Demagnetizing Field Analysis*

In this section, the reverse field distribution on the permanent magnets is determined. This is compared with the anticipated intrinsic coercivity of the permanent magnet material. It is demonstrated that a substantial margin against demagnetization, possibly due to thermal or radiation effects, exists in the magnetic design. Figure 6 illustrates the reverse field on the permanent magnet (the calculations were performed with $B_r = 1.35$ T and $\mu_{||}$=1.04). At the highest field regions the magnet material is potentially subject to demagnetization. Demagnetization occurs locally in regions of the magnet material where the reverse field (opposite the magnetization direction) $H > H_{cj}$, where $H_{cj}$ is the intrinsic coercivity of the permanent magnet material. The value of $H_{cj}$ depends upon the magnet grade and varies with temperature (the value decreases with higher temperatures).

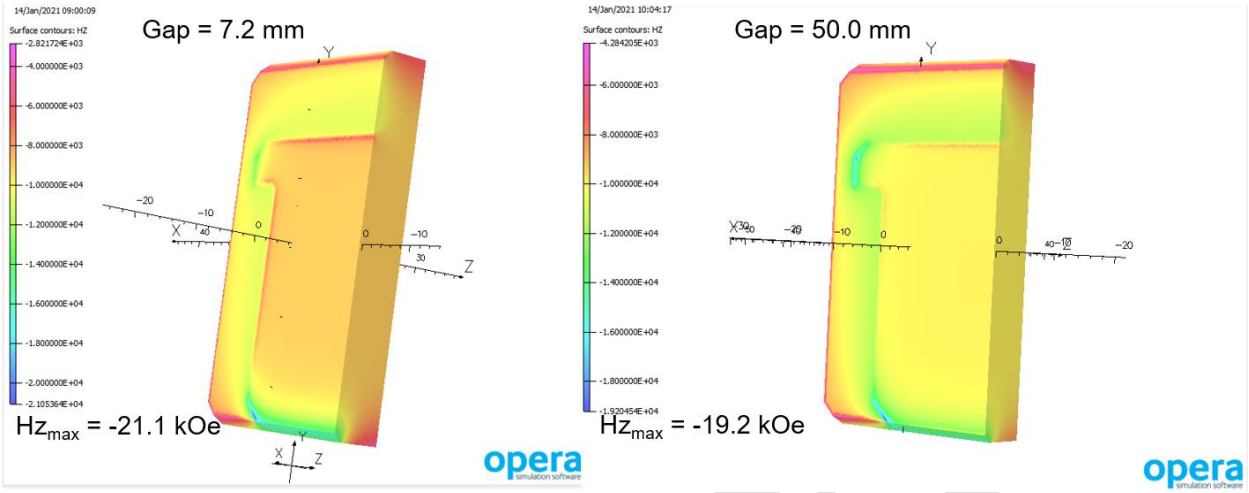


**Figure 6. OPERA3D model showing the magnetic field strength in the x-direction at the surface of the permanent magnet. The results are shown at minimum gap on the left and at large gap on the right.**

The issue of demagnetization must be considered within the context of magnet grade and temperature. For the LCLS-II-HE project, the minimum intrinsic coercivity is specified in the magnet material technical specification as being greater than 21 kOe in the bulk and 26 kOe near the surface (depth > 1mm). This is consistent with the magnet grades that were used for the LCSL-II undulators, which include a grain boundary diffusion process to enhance $H_{cj}$ near the surface of the magnets.

Figure 7 shows the distribution of $-H_z$ in the permanent magnet material for minimum gap (7.2 mm) and large gap (50 mm). As expected, the reverse field in the bulk of the material is higher at open gap than at closed gap. However, as can be seen from Figure 6, the peak value of the reverse field is higher at small gap with a small concentration near the corners of the pole chamfer features. These small regions with high reverse field are not visible in Figure 7 since their volume fraction is small. In order to get a better view of the high reverse field regions in the magnet, Figure 8 shows the fraction of nodes with the reverse field above a chosen field strength value, $H_{lim}$ (the left and right plots correspond to 7.2 mm and 50.0 mm gaps respectively). The node fraction quantity is a good approximation for the volume fraction since a uniform element size is used to mesh the entire permanent magnet in the simulation. From the plot it can be seen that for volume fractions greater than $10^{-5}$ (more than an order of magnitude relative to the required $B_{eff}$ repeatability) the highest reverse field in the permanent magnet less than 19 kOe. For a depth of greater than 1 mm, the highest reverse field in the permanent magnet less than 14 kOe. Based on the BH curves for the LCLS-II permanent magnet material, it is conservatively assumed that the knee of the BH curve starts at 2 kOe less than $H_{cj}$, this leaves a minimum of 5 kOe margin relative to the specified intrinsic coercivity (21 kOe in the bulk and 26 kOe at depth < 1.0 mm). The temperature margin can be estimated using the temperature sensitivity of $H_{cj}$ for the permanent magnet material. For material grade used for the LCLS-II SXR undulators (Grade 776 DTP), the minimum $H_{cj}$ was specified as 26 kOe at in the surface layer at 20°C, which corresponds to $H_{cj}$ = 22.5 kOe at 50°C. Using this temperature sensitivity, a minimum margin of 1.5 kOe remains at 50°C (using

conservative assumptions), which is 15°C above the specified maximum allowable storage temperature for the undulators.

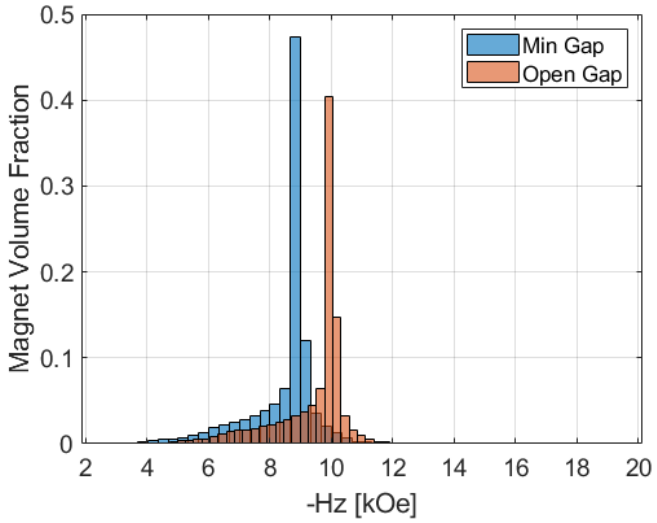


**Figure 7. Distribution of the demagnetizing field strength inside of the permanent magnet. The magnetic field strength is calculated at the centroid of the elements.**

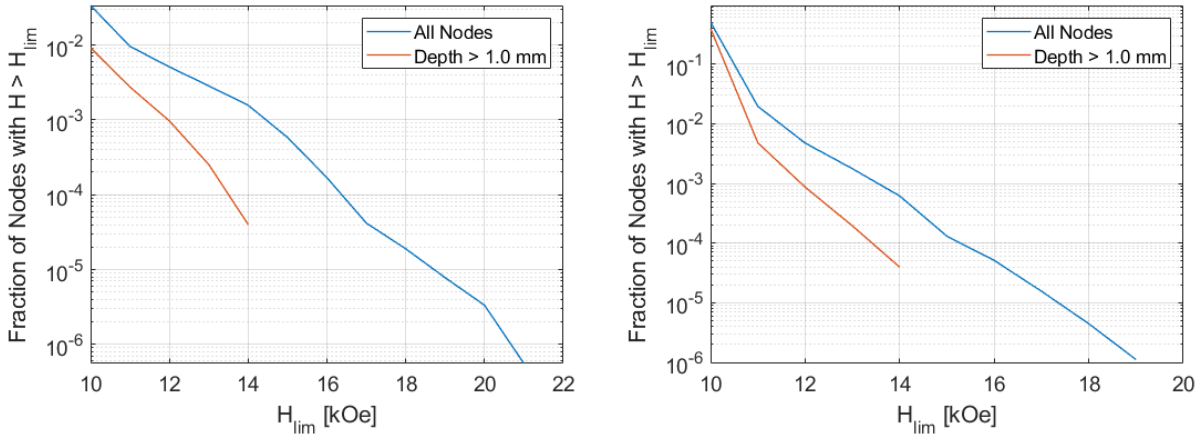


**Figure 8. Fraction of nodes with reverse magnetic field strength above the value shown in the x-axis. This is node fraction is representative of the volume fraction of material since a uniform element size is used to mesh the permanent magnet.**

## *Field Roll-Off Analysis*

For the field roll-off analysis, the effective field is computed at x values ranging from 0 to 3 mm in steps of 0.5 mm. Figure 9 shows the calculated field roll-off at the minimum and maximum values of the operational gap range. A 4$^{th}$ order polynomial is used to fit the data points in order to obtain a

smooth result since "noise" on the order of $10^{-5}$ normalized units is present at the mesh refinement level of the analysis. The left plot on Figure 9 shows the results over the full range of x values. The red dashed lines represent the allowed tolerance band ($\frac{\Delta K}{K} < 1.6 \times 10^{-4}$ at x = $\pm$0.4 mm) as prescribed in the Physics Requirement Document (see Table 1). The black dashed lines represent the region of interest (x = $\pm$0.4 mm). The right plot on Figure 9 shows a close-up view of the results. This demonstrates that the design meets the physics requirement with substantial margin for the highest roll-off case, which occurs at the maximum gap.

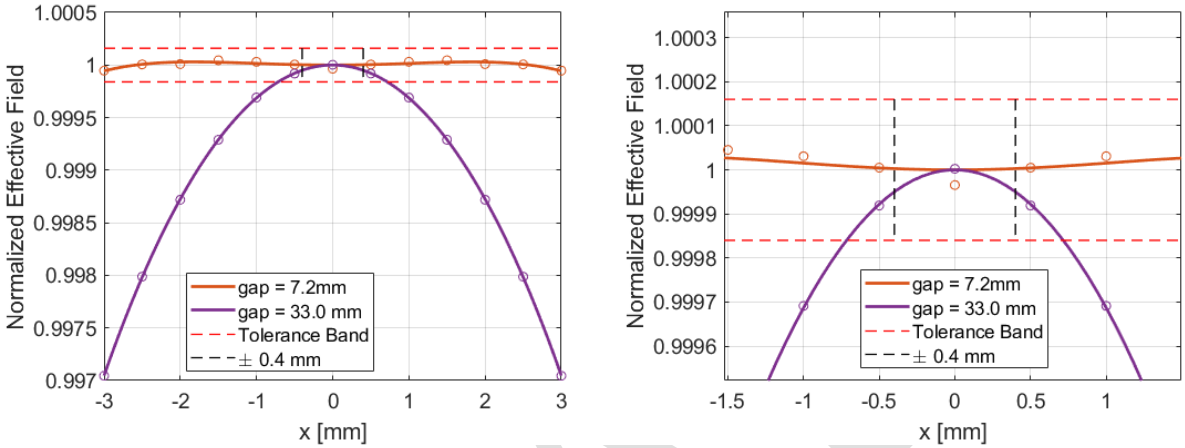


**Figure 9. Field roll-off along the x-axis at the minimum and maximum operating gaps. The tolerance bands correspond the specified physics requirements at x = ±0.4 mm.**

## *Magnetic Force Analysis*

The magnetic force on the poles and permanent magnets is calculated using the OPERA3D model. Table 5 shows the vertical force on individual poles and magnets and the total force across the gap of the undulator at the minimum and maximum operating gaps. A positive value corresponds to force towards the centerline of the undulator (into the gap), while a negative force corresponds to a force away from the centerline of the undulator (away from the gap). The maximum force across the gap of the undulator is 92 kN.

**Table 5.**

| Gap [mm] | Pole Force | Magnet Force | Undulator Force |
|---|---|---|---|
| 7.2 | + 830 N | - 50 N | + 92 kN |
| 33.0 | + 220 N | - 200 N | + 2.4 kN |

## *Design Verification and Case Studies*

In this section, the design verification process is described and a case study on the effect of pole saturation is presented. In order to verify the accuracy of magnetic analysis, two approaches are taken. First, the calculations are performed with the SXR geometry using OPERA3D, and the results are compared to actual measured values from the SXR production. For the second method, the HE-SXR model is solved using a different calculation method with the Radia package.

For the first validation method, LCLS-II SXR undulator measurements are compared to the OPERA3D calculations. For the SXR production undulators, the average gap at which a K value of 5.43 was achieved was found to be 7.77 mm. An OPERA3D calculation at this gap gives a K value of 5.37, when using the average magnet properties for the production of $B_r = 1.35$ T and $\mu_{||}$=1.04. For this case, the OPERA3D model underestimates the actual measured value by 1.1%. This gives a high level of confidence in the modeling approach and validates the choice of 2.5% calculated margin on Beff for the permanent magnet material specification.

For the second validation method, Radia is used to calculate the effective magnetic field using the same geometry and materials properties as for the OPERA3D model. Figure 10 shows the ¼ period representation of the Radia model that is used. The Radia model gives an effective value of 1.840 T, which is consistent with the value of 1.841 T that is obtained with OPERA3D (see line 2 in Table 3).

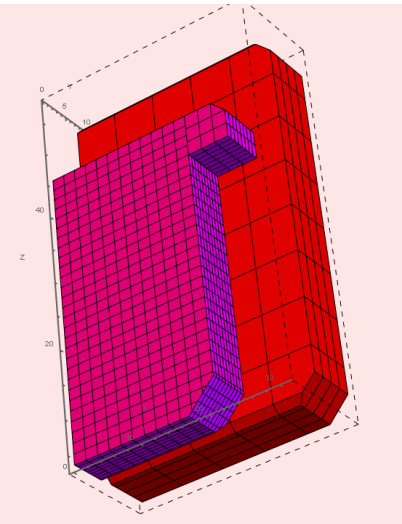

**Figure 10. Radia model of the pole and magnet with 1/8 symmetry. Symmetric boundary conditions in the longitudinal direction are used recursively to obtain a large enough structure so that the effective field value has converged.**

In order to validate the low saturation design, a case study for a systematic error that was found in the LCLS-II SXR pre-production unit is used. In this case, the systematic error was produced due to the assembly process. After all of the poles were assembled on the keepers, the odd magnets were first inserted into the assembly, then the even magnets were assembled. Due to the differences in axial magnetic force during installation of the even and odd magnets, systematic alternating gaps

were created as shown in Figure 11. An OPERA3D model (see middle diagram in Figure 11) was created to simulate this behavior. Excellent agreement was found between the model and the measured behavior of the undulator.

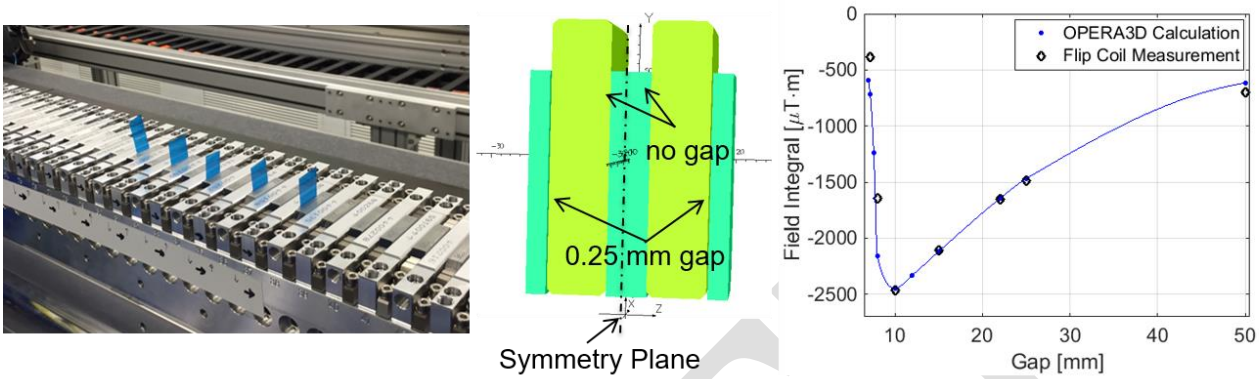


**Figure 11. Case study used to determine the effect of pole saturation on magnetic field errors. The left and center graphics show the systematic error that was discovered in the LCLS-II SXR pre-production unit. The plot on the right shows the excellent agreement that was obtained between the measured field integral and the model results.**

Due to this error, the field integral can be seen to increase in absolute value up to around 10 mm gap. At small gaps, the field integral error drops quickly since the poles become highly saturated. One can conceptually understand this by the fact that an error in the z-position of a pure permanent magnet undulator does not create a field integral error. A similar analysis was performed with the HE-SXR and HXR geometries. As can be seen in Figure 12, the gap at which the field integral error begins to decrease is significantly lower for both the HXR and HE-SXR designs when compared to the SXR design. This example is a good demonstration of the effect that the low saturation design can have on reducing highly non-linear gap dependent behavior in the undulator.

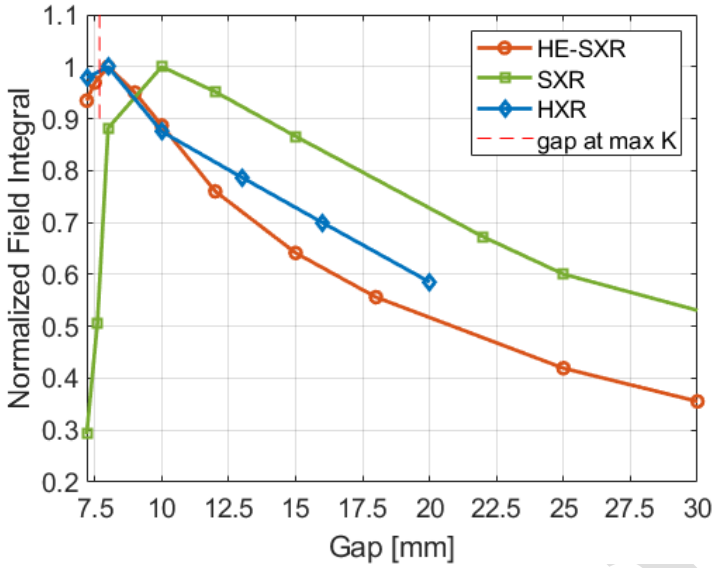


**Figure 12. Normalized field integral (normalized relative to peak value) as a function of gap for the pole saturation case study including the HE-SXR, SXR, and HXR undulators. As can be seen, the HE-SXR behavior is similar to the HXR behavior due to the reduced saturation in the poles relative to the SXR undulator.**

# 7. End Design

The objective of the magnetic termination is to minimize electron beam angle kicks and displacements at the entrance and exit. An example of an ideal termination is a series of scalar potential surfaces at values $0, \pm 0.25V_0, \mp 0.75V_0, \pm 1.00V_0$, spaced at the same intervals as the periodic poles and where V0 is the nominal full strength pole scalar potential. While the end magnetic structure can be configured to achieve this at a given gap, the scalar potentials will change as the gap is varied. The challenge is to find a configuration that keeps the end kick and displacements within appropriate bounds throughout the operating gap range.

In general, the electron beam will experience a systematic angle kick, α, and displacement, δ, as it enters the undulator field. These values must be evaluated against the second field integral requirement, which represents total displacement, Δ, where

$$\Delta = \alpha L + 2\delta$$

L is the length of the undulator and the factor of 2 accounts for the fact the systematic displacements at the entrance and exit are of the same sign (this is for true for the choice of even number of poles in the undulator). This behavior is illustrated in Figure 13 for a short undulator. In the left plot, the end displacement ($\delta$) is illustrated for a case where the angle kick is small (α). On the right plot, a case with a larger angle kick is shown and illustrated with the dashed lines. For a long undulator, even a small angle kick can lead to a large drift in the displacement.

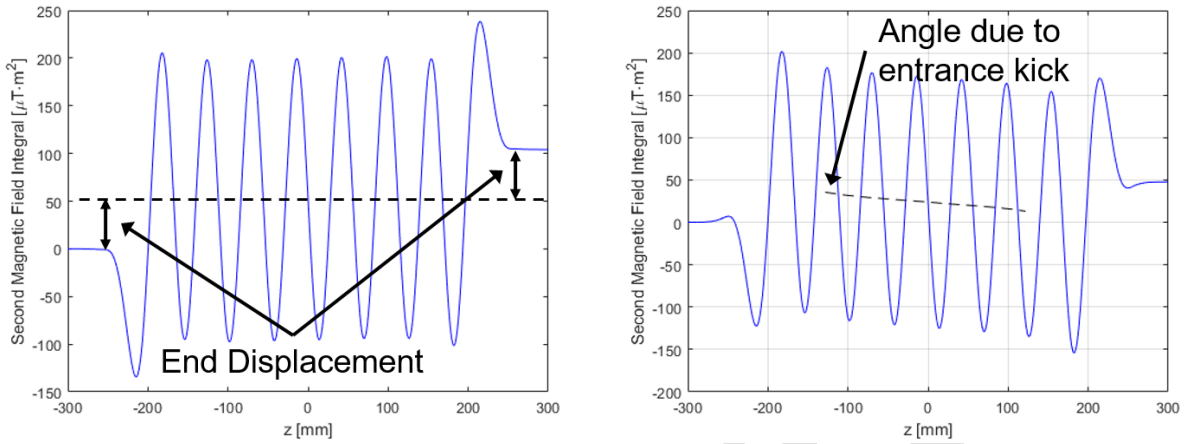


**Figure 13. Illustration of the displacement and angle kick at the ends of the undulator. The plot on the left shows an example with a relatively large end displacement (second field integral end jump), while the plot on the right shows an example with a relatively large end angle kick (first integral end jump).**

For the optimization of the ends, the target is to minimize the total displacement Δ, to ensure that the magnetic field at the first pole is close to zero (this acts as a field clamp and minimizes the stray field), and to minimize the deviation from the full field strength by the fourth pole. Figure 14 shows the OPERA3D model that is used to optimize the end design. It represents a 20 pole undulator[3] with 1/8 model symmetry. For the initial optimization work, the periodicity of the pole and magnet geometry was maintained for the entire structure and only the height of the first three magnets were varied. This is the approach that was used for the LCLS-II SXR and HXR undulators. While solutions that meet the requirements could be obtained, they did not provide significant margin. Therefore the parameter space was expanded to allow for modification of the thickness of the last two poles and the inclusion of three different tuning slugs (small horizontal, large vertical, and large horizontal slugs). These are illustrated in Figure 14.

[3] A separate study was performed to determine the minimum number of poles required for convergence to the long undulator result. A mesh refinement study was also performed to determine the appropriate mesh size for the optimization process and final result calculations.

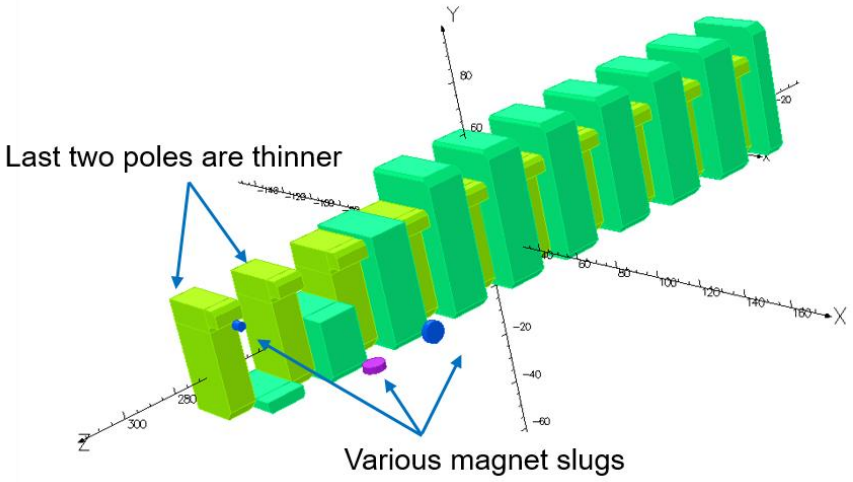


**Figure 14. Illustration of the magnetic end model in OPERA3D. The model simulates a 20-pole undulators and includes the following optimization parameters: heights of last three magnet blocks, thickness of last two poles (same value is selected for both), and three different permanent magnet slugs.**

For the optimization process, the Gauss-Newton algorithm is used with a constrained least squares method. The objective is to minimize the end kick (first integral end jump), the end displacement (second integral end jump), and the on-axis field at the first pole z location. This is determined for six different gaps (7.2, 8.0, 9.0, 15.0, 22.0, 33.0 mm), giving a total of 18 individual objectives, $\varphi_i$. The sum of the weighted squares of the individual objectives is the final objective function, $\emptyset = \sum_i w_i \varphi_i^2$. In order to determine the next iteration for the solution, a gradient approach is used. For this, a sensitivity matrix is created by perturbing the initial solution for each parameter, $\gamma_i$, at all gaps in the analysis. For example, the first end magnet height will be increased by 1 mm and the solution will be determined with this configuration for all gaps. This will then be repeated for the remaining control parameters. Since there are more individual objectives than parameters, a least squares method is used to find the updated parameters that minimize the objective function. This process is repeated until an acceptable solution is found. The process is as follows:

1. Calculate individual objectives, $\varphi_i$, with initial parameters $\gamma_i$ (these are also the residuals, $r_i$, since the target for the three objectives is zero)
2. Solve the end design model for all gaps (6) with, $\gamma_{i,\delta} = \gamma_i + \delta\gamma_i$ (7 maximum parameters)
3. Create sensitivity matrix, S, with components $\frac{\partial \varphi_i}{\partial \gamma_j}$
4. Calculate updated parameters $\gamma_{i+1} = \gamma_i - lsqlin(wS, wr)$, where $lsqlin$ is a bounded least squares method and $w$ is a vector containing the weights, $w_i$, of each individual objective
5. Repeat this until an adequate solution is found

In practice, the sensitivity matrix was not always updated for calculation of the solution since it has a heavy computational burden. At different iterations the full parameter space was also not always

used. In fact, the final solution only uses five of the available seven parameters. Some observations from the optimization process are as follow:

- The fast changing behavior of the first integral at small gap was mainly sensitive to the variation in height of magnet 3
- By setting the height of magnet 3 to minimize the small gap variation of the entrance / exit kick, the second integral could not be reduced sufficiently by only adjusting the heights of magnets 1 and 2
- Magnet slugs could be introduced to adjust the entrance / exit kick, but they are not effective at adjusting the second integral with a single set of slugs (this could be done with slugs at two locations spaced by a larger distance)
- The change in thickness to the first / last pole has little effect since this is a zero potential pole
- The change in thickness to the second / second-to-last pole gives sufficient freedom to adjust the second integral jump while maintaining the height of magnet 3 at an appropriate level to minimize the fast change in entrance / exit kick at small gap

Figure 15 shows the magnetic field and second field integral results for the final end configuration. The magnetic field under the fourth pole deviates by less than 0.5% of the periodic field. Figure 16 shows the final results for the individual end kicks and displacements. Figure 17 shows the final results for the total second field integral. The total second integral is less than 40 μTm², which gives significant margin relative to the requirement of 200 μTm². Table 6 shows the final dimensions for the end poles and magnets. The vertical magnet slug that is referenced in Table 6 is shown in purple in Figure 14.

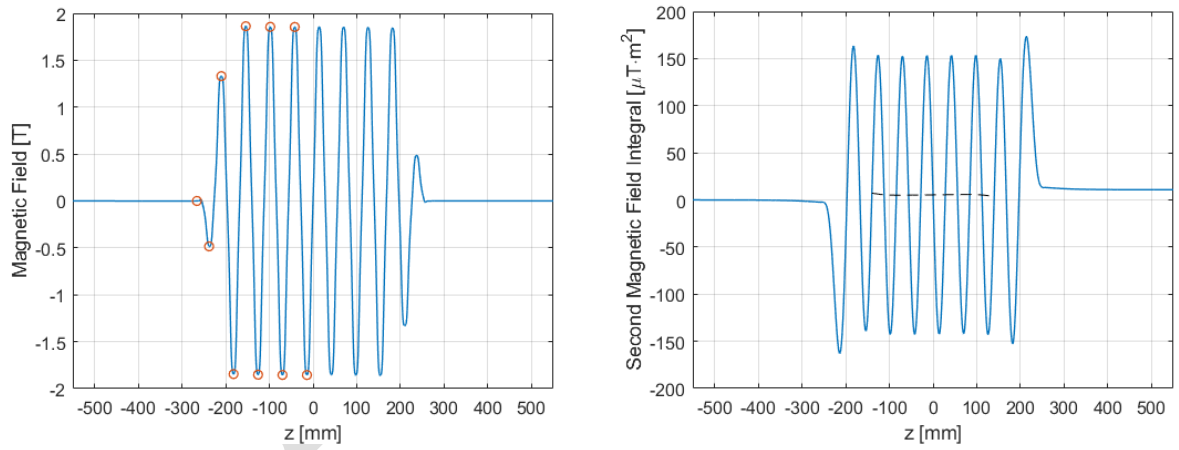


**Figure 15. Magnetic field (left) and second magnetic field integral (right) for the baseline design as a function of z.**

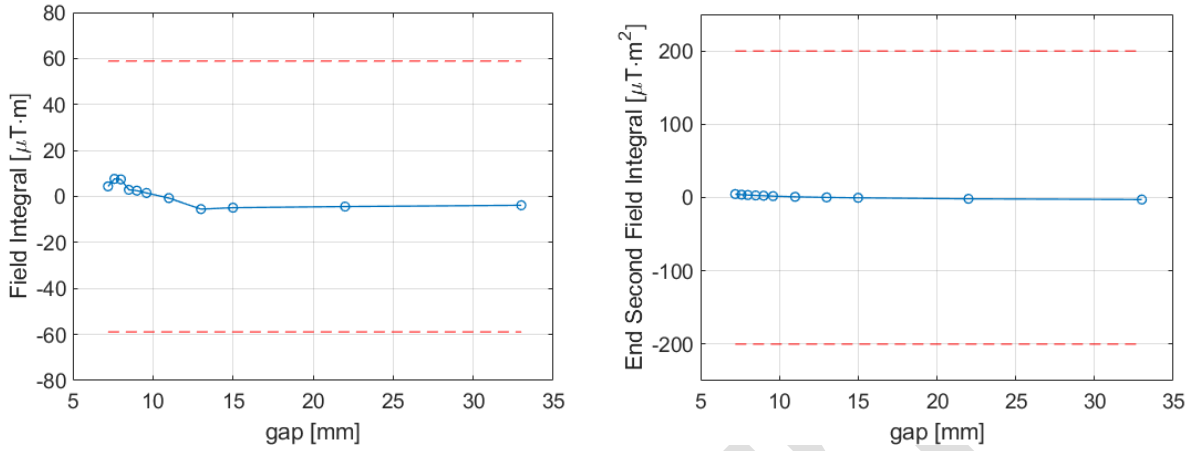


**Figure 16. End kick field integral (left) and end second field integral displacement (right) as a function of gap for the baseline end design.**

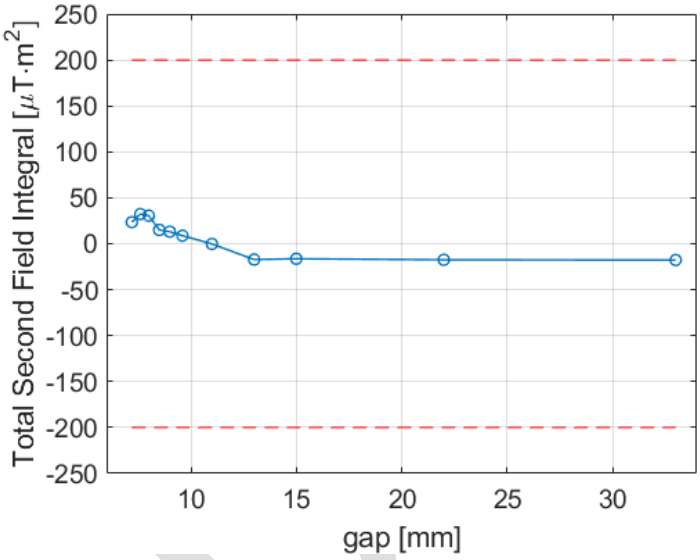


**Figure 17. Total second field integral for the end design (expanded for full-length undulator) as a function of gap. The dashed lines show the allowed value based on the physics requirements.**

**Table 6. Dimensions for the end design features.**

| Feature | Dimension |
|---|---|
| Magnet 1 Height | 4.23 mm |
| Magnet 2 Height | 23.46 mm |
| Magnet 3 Height | 43.50 mm |
| Pole 1 & 2 Thickness | 10.38 mm |
| Vertical Magnet Slug diameter × length | 7.9 mm × 2.5 mm |

# 8. Tuning Method Analysis

Tuning for the HE-SXR undulator will be performed using the same methods that were qualified in the LCLS-II HXR and SXR undulator production. For vertical field correction, these include vertical pole position adjustments and small permanent slugs near the base of the pole (the large slugs near the surface of the keeper can also be used). For horizontal field correction, pole canting and vertical and horizontal magnet slugs near the surface of the keeper can be used. Figure 18 shows the CAD model of the keeper which includes designed features for the various tuning methods. On the left, the pole adjustment mechanics and small slugs near the base of the pole are shown. In the middle, the horizontal slugs near the keeper surface are shown. In the right, the vertical slugs near the keeper surface are shown. Figure 19 shows the simulated gap dependence for the first field integral for the various tuning methods. The left plot shows the vertical tuning methods: pole vertical adjustment (blue) and small slugs at pole base (red). The pole adjustment corresponds to a 25 μm adjustment on both the top and bottom undulator jaws, while the slugs correspond to a stack four magnet slugs with 1/8" diameter and 1/8" length (applied in symmetric manner). The right plot in Figure 19 shows the horizontal tuning methods: pole cant adjustment (blue), vertical slugs near keeper surface (red), and horizontal slugs near keeper surface (yellow). The pole cant adjustment corresponds to a 2 mrad adjustment on both the top and bottom undulator jaws, while the magnet slug correction correspond to a stack four magnet slugs with 5/16" diameter and 1/8" length (applied in symmetric manner).

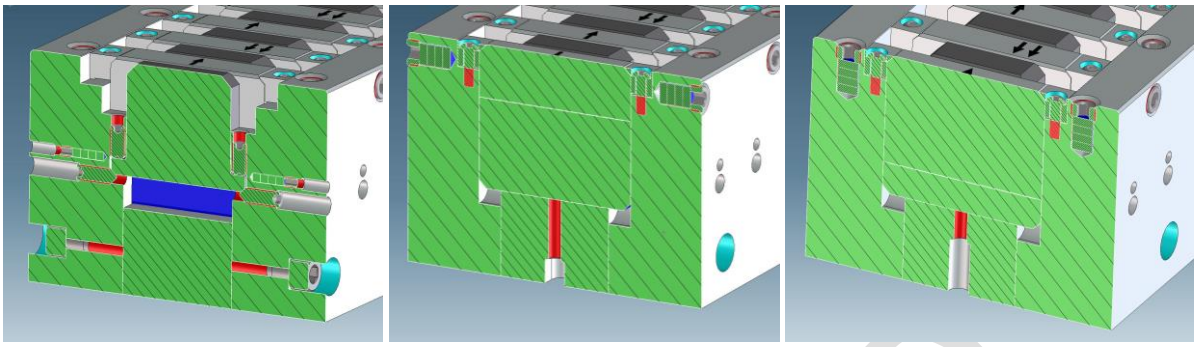

**Figure 18. CAD model of the HE-SXR undulator magnet module showing the tuning features. The graphic on the left show the pole adjustment features and the small slugs at the base of the pole. The graphic in the middle and the right show the horizontal and vertical slugs near the keeper surface, respectively.**

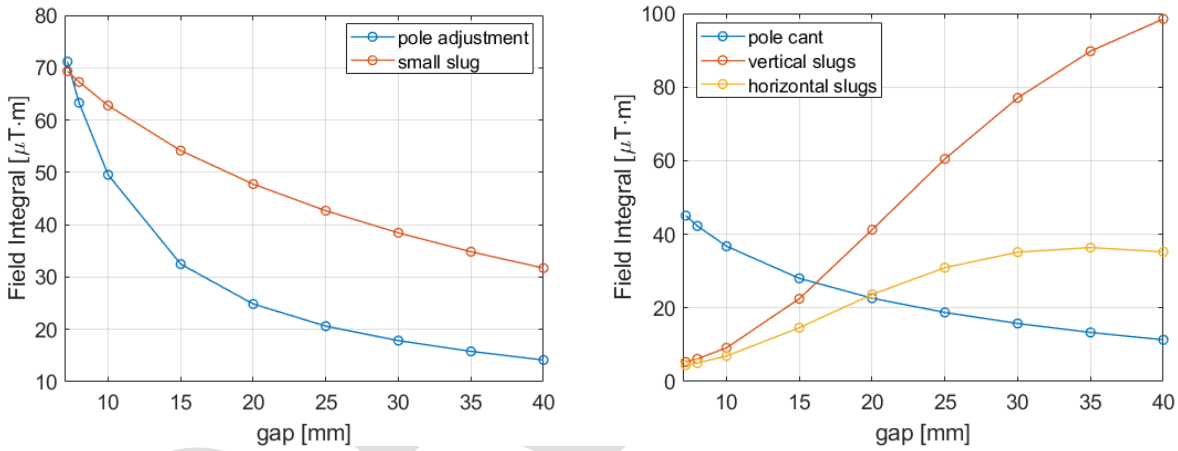


**Figure 19. Field integral response from the tuning methods as a function of gap. The left plot shows the response for the vertical tuning methods, while the right plot shows the response for the horizontal tuning methods.**

# 9. Reference Documents

- LCLS-II-HE-1.3-PR-0049-R0 - LCLS-II-HE SXR Undulator Systems Physics Requirement Document
- SXR magnetic design – LBNL Engineering Note 10994E
- HXR magnetic design – LBNL Engineering Note 10988E
- Magnet material specification – LC-1006-1820
- Pole material specification – LC-1006-1866